Insights into photocatalytic inactivation mechanism of the hypertoxic site in aflatoxin B1 over clew-like WO3 decorated with CdS nanoparticles

Jin Mao[a], Peiwu Li[a,c,**], Jinming Wang[b], Huiting Wang[a], Qi Zhang[a], Liangxiao Zhang[a], Hui Li[a], Wen Zhang[a], Tianyou Peng[b,*]

[a] National Reference Laboratory for Agricultural Testing P.R.China, Key Laboratory of Detection for Mycotoxins (Ministry of Agriculture), Laboratory of Quality & Safety Risk Assessment for Oilseed Products (Ministry of Agriculture),Oil Crops Research Institute, Chinese Academy of Agricultural Sciences, Wuhan 430062, China
[b] College of Chemistry and Molecular Sciences, Wuhan University, Wuhan 430072, China
[c] Key Laboratory of Biology and Genetic Improvement of Oil Crops (Ministry of Agriculture), Oil Crops Research Institute, Chinese Academy of Agricultural Sciences, Wuhan 430062, China

ARTICLE INFO

ABSTRACT

Aflatoxin B_1 (AFB$_1$) is regarded as a main biological pollutant with high toxicity, carcinogenicity and teratogenicity, and the double bond (C8=C9) of its terminal furan ring is the key hypertoxic site. Although semiconductor photocatalysis has been proposed to be a potential way of reducing or inactivating the toxicity of AFB$_1$, the reaction mechanism of reactive oxygen species with the hypertoxic site has not been defined so far. Herein, a kind of all-solid-state Z-schematic composite was fabricated by depositing CdS on the surface of clew-like WO$_3$, which can sharply reduce the toxicity of aflatoxin B$_1$ in aqueous solution under visible light irradiation according to the cytotoxicity test result. On the bases of high resolution mass spectrum (HRMS), radical trapping test and ^{18}O isotope-labeling studies, it can be concluded that the preferentially inactivating the C8=C9 site by the addition reaction of hydroxyl radical was the main pathway for the detoxification of aflatoxin B$_1$. Furthermore, density functional theory (DFT) calculations were applied to reveal the reaction mechanism and verify that the hydroxyl radicals were most likely to react with the C9 site, and then form AFB$_1$-9-hydroxy. This work provides in-depth insights into the inactivation mechanism of hypertoxic site in AFB$_1$, and the design of efficient photocatalysts for alleviating the risk of toxic pollutants.

1. Introduction

Environmental pollutants with high toxicity and stability from chemical, physical and biological source have become a worldwide concern. Aflatoxin B_1 (AFB$_1$), as one of most important biological pollution, is a highly toxic, mutagenic, and carcinogenic secondary metabolite produced by fungus from the soil and agricultural products [1]. It can contaminate the soil and water source through raining and wet processing, and then directly influence health of ecosystems and bring serious threats to human [2,3]. The highly toxic activity of AFB$_1$ is ascribed to its extremely stable chemical structure, which is composed of the double furan rings and coumarin [1,4]. And the double bond of terminal furan ring in AFB$_1$ (C8=C9 site in the Scheme 1) is the key toxic and carcinogenic site, which can be transformed to AFB$_1$-8,9-epoxide in the body, and then combine with DNA, glutathione S-transferase or N7 guanine to form adducts [4–6]. These adducts such as

AFB$_1$-DNA can induce the gene mutations that prevent the normal action of tumor suppressor genes, and promote cancer to develop and grow [5,6]. It was found that reducing aflatoxins exposure to non-detectable levels could decrease hepatocellular carcinoma cases by about 23% [7]. Therefore, on condition that the hypertoxic site (C8=C9 double bond) of AFB$_1$ was destroyed or inactivated, the toxicity and carcinogenicity could be sharply diminished.

Due to high stability of AFB$_1$, traditional strategies for the AFB$_1$ detoxification often required harsh condition and/or more energy consumption, *e.g.*, gamma ray radiation [8], ozone [9] and enzymatic detoxification [10]. Although most of attentions had been paid to the efficiency of detoxification and identification of intermediate product, the comprehensive studies on mechanism of detoxification reaction such as confirmation of reactive groups, interaction sites were scarce. Recently, photocatalysis had been proved to exhibit activity on AFB$_1$ mitigation in aqueous solution by our previous report [11]. Moreover, it
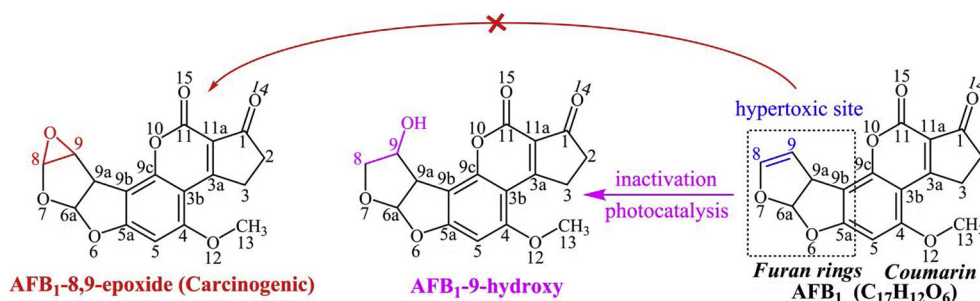
Scheme 1. The structure of AFB_1, AFB_1-8,9-epoxide and AFB_1-9-hydroxy.

was supposed that one of initial intermediate products (named as AFB_1-9-hydroxy) formed through photocatalytic reaction on the hypertoxic site of furan ring in AFB_1 (shown in Scheme 1). However, little specific mechanism information about this photocatalytic inactivation of toxic site in AFB_1 had been studied so far. Obviously, an in-depth research on reaction mechanism, especially on this key site that determines the carcinogenic toxicity of AFB_1, is desirable for our understanding about this issue and its application in future.

Because the photocatalytic reaction was performed in the present of water and oxygen conditions, several main reactive oxygen species (ROS) including hydroxyl radical ($\cdot OH$), superoxide radical ($\cdot O_2^-$) and hydrogen peroxide (H_2O_2) produced from H_2O and O_2 reacting with the photogenerated holes and electrons. In this case, the performance of photoreaction was determined by the type and amount of ROS, which depended on the properties of catalyst and the reaction conditions. Therefore, the analysis of ROS reaction was significant for revealing the photoreaction mechanism. Among these active oxygen species, $\cdot OH$ radical with admirably high reactivity was regarded as the most effective reactant for pollutants mitigation, which could be directly produced from the oxidation of H_2O or OH^- and indirectly produced from $\cdot O_2^-$ on the surface through multi-step reactions. Generally, the $\cdot OH$ radical reactions with organic pollutants were known as two reactions pathway: addition to unsaturated carbon bonds (C=C) and H-atom abstraction from C–H or O–H bonds. In this case, it seemed that AFB_1-9-hydroxy was the product of $\cdot OH$ radicals addition reaction on the C8=C9 double band in AFB_1, however, the actual role of $\cdot OH$ radicals and other ROS on the toxic site of AFB_1 required more evidences.

Therefore, the aim of this study is to obtain more profound understanding on photocatalytic inactivation mechanism of the hypertoxic site in aflatoxin B_1. Firstly, development of photocatalytic system with high productivity of ROS such as $\cdot OH$ radicals is essential. Among various photocatalytic systems, the all-solid-state Z-schematic system has been regarded as a commendable system for environmental remediation application, which can promote the separation of photogenerated charges and utilize the excellent redox potential at two reaction sites [12–16]. As a visible light responding catalyst, tungsten oxide (WO_3) with low cost, environment-friendly and stability is regarded as an excellent candidate for constructing Z-scheme composites. Most important, WO_3 has an applicable bandgap (ca. 2.6 eV) with a more positive valence band (VB), and the holes on VB can directly oxidize the OH^- or H_2O to $\cdot OH$ [17,18]. Current researches on Z-scheme system associated with WO_3 mainly focuses on one-dimensional (1D) and two-dimensional (2D) structures such as nanosheets [19], nanorods [20,21], nanowires [22] and nanoparticles [23], which have been widely applied in pollutants mitigation and solar energy conversion. Compared with 1D and 2D structural semiconductors, oriented 3D micro/nanostructures often possess unique photoelectric and catalytic properties, which could provide more charge transfer pathways and more active sites [24–27]. However, due to the special properties of tungsten element, it is difficult to control the morphology of WO_3 into well-defined 3D nanostructure through facile and mild methods without specific template and harsh reaction conditions [28].

Therefore, it is challenging to fabricate the uniform, stable and 3D nanostructured WO_3 in the mild conditions, and then construct Z-schematic composites for photocatalytic application.

To construct the Z-scheme composites, the band gap of two components must be suitable, indicating that it is necessary to select a semiconductor photocatalyst matched with WO_3. Cadmium sulfide (CdS) with large light-harvesting capacities, more negative CB potential and high-energy conversion efficiencies is regarded as a candidate for constructing Z-scheme composites. Moreover, it was found that CdS nanoparticles could be uniformly deposited on the surface of WO_3 through facile precipitation method to construct efficient Z-scheme composites [27]. Therefore, using CdS to form Z-scheme composite with WO_3 may be an appropriate strategy. Most importantly, combination of analytic technologies is a good way to study the mechanism and pathway of ROS reaction with pollutant. The detailed product analysis by High Resolution Mass Spectrum (HRMS), reactants with stable isotope labeling and theoretical calculation are effective measures. By these approaches, the deeper and better understanding can be gained from both theoretical and experimental analysis.

Herein, the photocatalytic inactivation mechanism of the hypertoxic site C8=C9 double band in AFB_1 was revealed. A highly efficient Z-schematic system composed of clew-like WO_3 and CdS nanoparticles was facilely fabricated, which was proved to produce more $\cdot OH$ radicals that preferentially inactivate the hypertoxic site of AFB_1 in aqueous solution under visible light irradiation. Most of all, the reaction mechanism of $\cdot OH$ radical on the toxic site C8=C9 double band of AFB_1 were discussed systematically through the structure identification of intermediates, ^{18}O isotope labeling experiments and DFT theoretical calculations for the first time. The reasons of enhanced performance were also investigated by the solar light adsorption, photo-generated charges separation efficiency, lifetime and photoelectric property of as-prepared composites. Finally, the toxicities of main intermediates after photocatalytic treatment were also evaluated.

2. Materials and methods

2.1. Chemicals and reagents

All chemicals and reagents were analytical grade without further purification treatment, which were purchased from Sigma-Aldrich or Sinopharm Chemical Reagent. In addition, chromatographic grade reagents such as methyl alcohol, acetonitrile were purchased from Sigma-Aldrich for high-performance liquid chromatography (HPLC) and HRMS. The ultrapure water derived from a Milli-Q SP Reagent Water system was used for all solution.

2.2. Material synthesis and characterization

Clew-like WO_3 were prepared by a microwave-assisted hydrothermal method similar to the previous reports with modifications [29,30], and without fluorine-doped tin oxide (FTO) substrate. Firstly, 10% HCl (wt%) was slowly added into 100 mL 10 mM sodium tungstate

solution until no more precipitate generated. The precipitate was centrifuged and washed with ultrapure water for three times, then dispersed in ultrapure water to form a suspension. After that, 10 mM oxalic acid was added into the above suspension under powerfully stirring, and then the same amount CH_3COONa as capping agent was added after that the suspension became transparent. The pH value of solution was adjusted to 0.8 by HCl solution, and then the solution was transferred into a tetrafluoroethylene tube (50 mL), and heated in a microwave oven (Mars X, CEM Corporation, USA). The temperature was from 25 °C to 180 °C in 20 min under the microwave power of 800 W, and then kept at 180 °C for 1 h under ordinary pressure. After reaction, the solid was washed with ethyl alcohol and ultrapure water for three times, respectively. Finally, the solid were calcined at 500 °C for 1 h to transform crystal and remove the organic residues.

The CdS/WO_3 composites were synthesized *via* a simple precipitation method. In general, 0.1 g of as-prepared WO_3 was dispersed in 50 mL of ultrapure water, and a certain volume (0 mL, 0.5 mL, 1.0 mL, 2 mL and 4 mL) of 0.05 M $Cd(CH_3COO)_2$ solution was added in suspension drop by drop with stirring. After 20 min, the same volume of 0.05 M Na_2S solution was added dropwise, and then kept stirring for 30 min. Finally, precipitates were washed several times with ultrapure water, and dried at 80 °C for 12 h for further characterization and photocatalytic test. According to the initial mass ratio (wt%) of CdS to WO_3, the $CdS-WO_3$ samples were noted as CW-3.61%, CW-7.22%, CW-10.83% and CW-14.44%. The actual mass ratio and specific surface area of the samples were shown in Table S2 in *Supplementary data*. The detailed morphological, structural and photoelectric characterizations of as-prepared catalysts can be also found in *Supplementary data*.

2.3. Photocatalytic measurement

The photocatalytic reaction was performed in a reaction cell (Pyrex glass) under visible light irradiation ($\lambda > 420$ nm), and the intermediates or products after photoreaction were identified by HRMS (Thermo Scientific Orbitrap Fusion hybrid mass spectrometer). The detailed information could be found in *Supplementary data*. Finally, the toxicity assessment was verified by the cell viability assay according to our previous work [31].

2.4. Theoretical methods

All of the calculations were performed with Gaussian 09 software [32]. Geometry optimization of all the minima and involved transition states were carried out at the B3LYP [33,34] level with the 6-31 + G(d,p) basis set for C, H and O. Default convergence criteria were used. The vibrational frequency calculations were conducted at the same level of theory as geometry optimization to confirm whether each optimized structure is an energy minimum. The solvent effects were considered using the polarizable continuum model (PCM) [35,36] with the as-phase-optimized structures as the initial geometries.

3. Result and discussion

3.1. Morphology and crystal phase analyses

Fig. 1a displayed that the as-prepared WO_3 after calcination presented uniform clew-like structure with diameter size of 6-7 μm, which was composed of a great deal of nanoblocks with length size of about 100–200 nm (Fig. 1b). From TEM image of Fig. S1a, it was found that the accumulational nanoblocks presented oval image, which could not be transmitted by light due to thick structure. However, thin nanoblocks could be observed clearly on the edge of WO_3 clew from Fig. S1b. To obtain further information of the microstructure, the HRTEM image (Fig. 3c) was demonstrated. The WO_3 showed obvious lattice fringes with a *d*-spacing of 0.37 nm that was ascribed to the (002) lattice plane of monoclinic WO_3 [27,38], which was coincident with the following XRD results.

The HRTEM of CW-10.83% composite was demonstrated in Fig. 3d. It could be clearly seen that two kinds of lattice fringe formed a tight connection, indicating that CdS nanoparticles with particle size of 4–5 nm *via* precipitation method were successfully located on the surface of the WO_3. The different lattice spacing values were 0.37 nm and 0.336 nm, which were consistent with the (002) lattice plane of monoclinic WO_3 and the (111) lattice plane of cubic CdS, respectively [27,39]. Furthermore, the EDS mapping of CW-10.83% showed that composite included the four elements (W, O, Cd and S), which were commendably dispersed in as-prepared composite. Above characterizations collectively indicated that CdS nanoparticles uniformly combined with WO_3, and this intimate combination between two semiconductors may facilitate photogenerated charges separation and transfer, which can be of benefit to enhance the photoactivities.

The XRD patterns (Fig. 2) indicated that the as-prepared sample derived from microwave assisted hydrothermal synthesis was the orthorhombic $WO_3\cdot1/3H_2O$ (JCPDF 87-1203) [29,37]. After annealed at 500 °C for 1 h, WO_3 transferred to the pure monoclinic phase (JCPDF 83-0951), which could be also found in the previous report [29]. The CdS sample with three main diffraction peaks could be ascribed to (111), (220), and (311) plane diffraction of the cubic phase (JCPDF 80-0019). Furthermore, it was found that no distinct diffraction peaks shifted in all CdS/WO_3 composites as shown in Fig. S2, indicating that the composites solely consisted of CdS and WO_3. No diffraction peaks of CdS were found in the CdS/WO_3 composites, which was due to low amount and relatively low XRD diffraction intensity of CdS. However, the peak intensity of CW-14.44% was weaker than the pure WO_3 after annealing, which may be due to that lower relative of WO_3 in composites, and CdS with weak crystallization on the surface of WO_3 blocks X-ray and coherent scattering [27]. In amplifying patterns of composites from $2\theta = 26°–27°$ (right of Fig. S2), the peak at about $2\theta = 26.6°$ became wider with the increase of CdS concentration, signifying that the more (111) plane of CdS exposed in samples. To identify the surface chemical compositions and valence states, the XPS results and analyses were presented in Fig. S3 and *Supplementary data*.

3.2. Photocatalytic efficiencies and photoelectric properties of catalysts

The efficiency of catalysts for catalyzing AFB_1 inactivation were investigated in aqueous solution under visible light irradiation. It was observed that the AFB_1 could not be reduced under visible light irradiation without catalysts or in the presence of catalyst without visible light irradiation. As shown in Fig. 3 a and Table S2, it was found with the increase of CdS content, the adsorption of AFB_1 faintly increased, and CW-10.83% showed the best activity compared with the single catalyst and other composites. With the content of CdS increasing, the catalytic efficiency enhanced gradually, which may be due to that better combination formed between WO_3 and CdS. However, when the concentration of CdS was up to 14.44%, the C_t/C_0 rate of AFB_1 decreased from 95.5% to 80.2%. This decrease may be caused by that the excessive of CdS could prevent the light absorption and photo-generated charges transfer of WO_3, and decrease the active sites on the surface of WO_3. Furthermore, the stability of as-prepared catalyst were the important properties for long-term utilization in practical applications. As shown in Figs. 3b and S4, it was worth noting that the slight reduced photocatalytic performance of CW-10.83% after four cycles, and the main peaks of XRD and XPS were not changed after long-term photoreaction. In addition, the element contents from XPS and the actual mass concentration from Inductively Coupled Plasma Optical Emission Spectrometer (ICP-OES) showed that there was no obvious change before and after long-term reaction (Table S3 and S4). This illustrated that the catalyst exhibited the well chemically and physically stability. In addition, it was found that the as-prepared composites could be conveniently separated from aqueous solution by centrifugation with 3000 rpm. Thus, above results indicated that CW-10.83% was
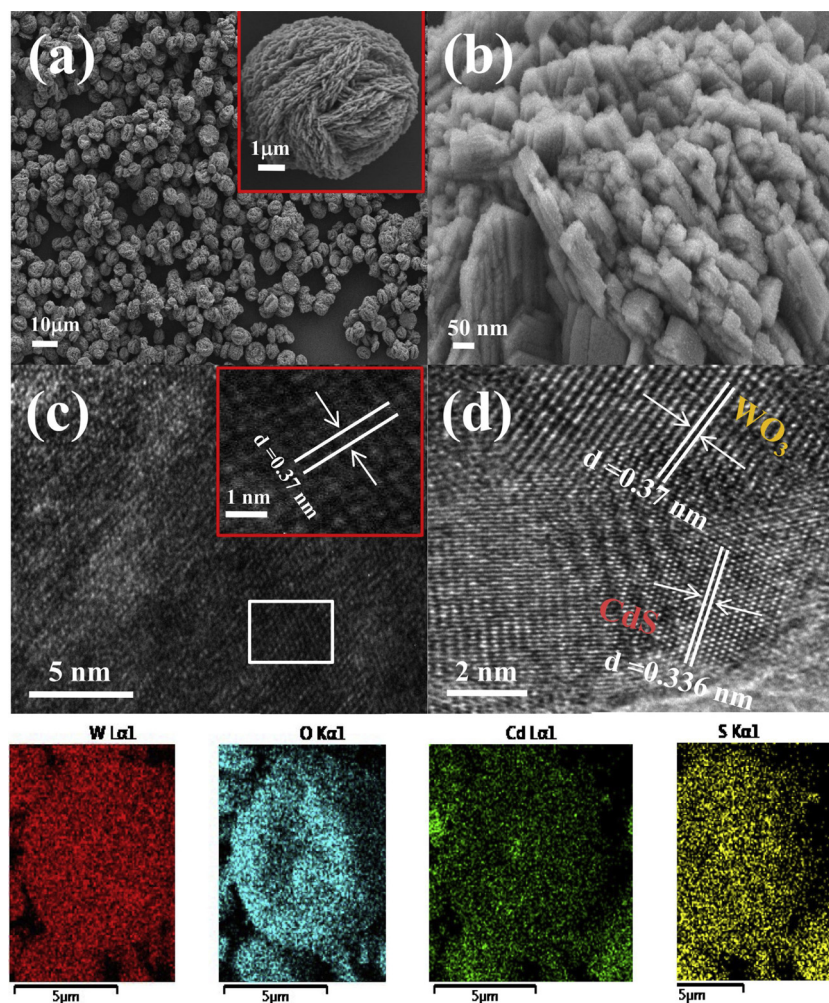
Fig. 1. SEM of WO$_3$ (a, b), HRTEM of WO$_3$ (c) and CW-10.83% (d), and W, O, Cd, S elements mapping image in below.
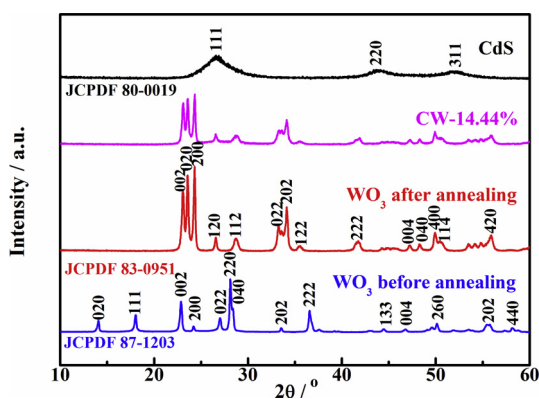

Fig. 2. XRD patterns of as-prepared WO$_3$, CdS and the composites.

an efficient catalyst and could be availably reused.

To investigate the reasons of enhanced photocatalytic activity, the photoluminescence spectra (PL) and transient PL decay curves were performed to evaluate the separation efficiency and lifetime of charges, respectively. From Fig. S5a, the strong emission peak at *ca.* 465 nm was ascribed to the fast recombination of photogenerated electron-hole pairs on the surface of WO$_3$, while the broad peaks between 500 nm and 550 nm were attributed to recombination of trapped charge carriers at surface defect of CdS [40]. The PL emission intensity of WO$_3$ was sharply quenched after CdS nanoparticles deposited, and the CW-

10.83% showed the weakest PL intensity, indicating that optimized concentration of CdS in composites could effectively decrease the recombination of photogenerated electrons and holes. Moreover, the transient PL decay curves (Fig. S5b) of catalysts were applied to evaluate the kinetics course of charges under light irradiation. After exponential fitting and calculating, the charge carrier lifetime of WO$_3$, CdS, CW-3.61%, CW-7.22%, CW-10.83% and CW-14.44% were 1.007, 1.566, 1.713, 1.943, 2.762 and 2.145 ns, respectively. The prolonged lifetime of charges can play a vital role in enhancing photocatalytic activity, in other words, more electrons and holes could take part in the photoreaction. From above characterizations, it could be concluded that the optimized content of CdS deposited on WO$_3$ were beneficial to charges separation and electron/hole transfer, and then enhance the photocatalytic performance.

The photoelectrochemical properties of catalysts were also evaluated by transient photocurrent and electrochemical impedance spectra (EIS). As shown in Fig. S5c, the transient photocurrent of catalysts on FTO during light on-off recycles repeated regularly, and the CW-10.83% displayed best photo-responsive performance by the intensity of generated photocurrent among these catalysts. It was found that the slight decrease of photocurrent curves with time, which was caused by two reasons, 1) the light source may spend a moment to reach stability, 2) the reduced interaction between catalysts and FTO in electrolyte solution under light irradiation. In addition, the EIS of CW-10.83% (shown in Fig. S5d) also presented smallest diameter of the Nyquist plots, indicating the lowered resistance of charges transfer after suitable combination between CdS and WO$_3$. Thus, the highest efficiency of
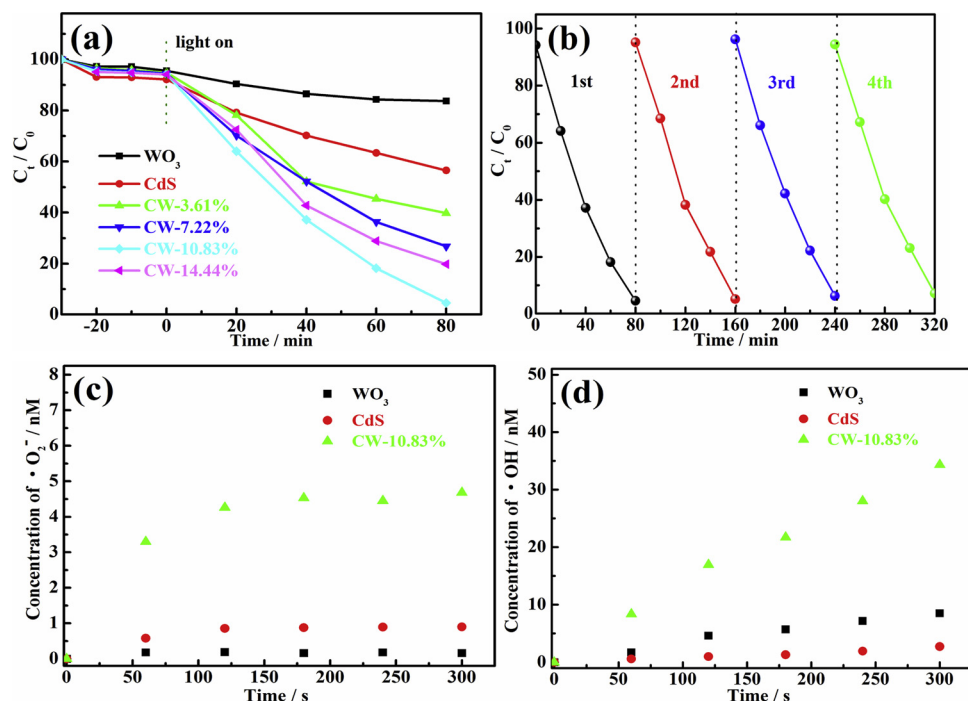
Fig. 3. Photocatalytic inactivation of AFB$_1$ over as-prepared catalysts under visible light irradiation (a), cycling tests for photocatalytic inactivation of AFB$_1$ over CW-10.83% (b), the $^{\cdot}O_2^{-}$ concentration (c) and $^{\cdot}OH$ concentration (d) measured from chemiluminescence method in the presence of Methoxy Cypridina Luciferin Analog and the coumarin fluorescence probe method over CW-10.83% under visible light irradiation, respectively.

photo-responsive performance and best conductivity were other important evidences for the enhanced photocatalytic activities of CW-10.83%.

3.3. Photocatalytic inactivation mechanism on C8═C9 in AFB$_1$

Detection of main ROS in photoreaction was the important evidence to analyze the mechanism of photocatalytic inactivation. Fig. 3c and d showed the concentration of $^{\cdot}O_2^{-}$ and $^{\cdot}OH$ radicals as a function of time according to previous methods [41]. The growth of $^{\cdot}OH$ radicals accumulated with time, which was different from the curve of $^{\cdot}O_2^{-}$ radicals. These results in growth feature were due to the difference in two detection methods. The amount of $^{\cdot}OH$ radicals was measured from the accumulation of reaction product, while the amount of $^{\cdot}O_2^{-}$ radicals were detected at each moment that contained competitive reactions between degeneration and generation [41]. From Fig. 3c and d, it could be found that CW-10.83% presented the much better productivity of $^{\cdot}OH$ and $^{\cdot}O_2^{-}$ radicals generation during the photoreaction compared with CdS and WO$_3$, which was beneficial to explain the enhanced performance over CW-10.83% for toxic site inactivation.

Fig. 4 presented the total ion chromatogram of photocatalytic products of AFB$_1$ in aqueous solution over CW-10.83%. It could be found

that the concentration of AFB$_1$ decreased with irradiation time, indicating that the photoreaction occurred. The four kinds of main intermediate products formed regularly, and the intermediates at retention time of 5.37 min, 7.84 min and 8.39 min were ascribed to C$_{17}$H$_{14}$O$_7$, C$_{14}$H$_{16}$O$_4$ and C$_{12}$H$_{10}$O$_4$, respectively, which can be also found in our previous work under the same optimized extraction and MS conditions [11]. However, there was a new intermediate product (C$_{14}$H$_{14}$O$_3$) that could not found in previous study, which might be due to that the different number of active radicals formed in presence of different catalysts. The molecular structure of C$_{14}$H$_{14}$O$_3$ were proposed according to the MS/MS spectrum and the fragmentation formation (Fig. S6).

The nominal level (NL) of intermediate products from Fig. 4 were collected in Table 1, which reflected the responsive value and concentration of different target molecules. Obviously, the C$_{17}$H$_{14}$O$_7$ (AFB$_1$-9-hydroxy) as a main intermediate was detected, and its concentration increased from 0 min to 80 min, and then decreased with irradiation time. This indicated that the double bond of furan ring (C8═C9) may be easily and preferentially attacked by active radicals such as $^{\cdot}OH$ during the photoreaction to form AFB$_1$-9-hydroxy. After 80 min irradiation, due to only a little AFB$_1$ in the solution from Fig. 3a and Fig. 4, the inactivation of AFB$_1$ to C$_{17}$H$_{14}$O$_7$ (AFB$_1$-9-hydroxy)
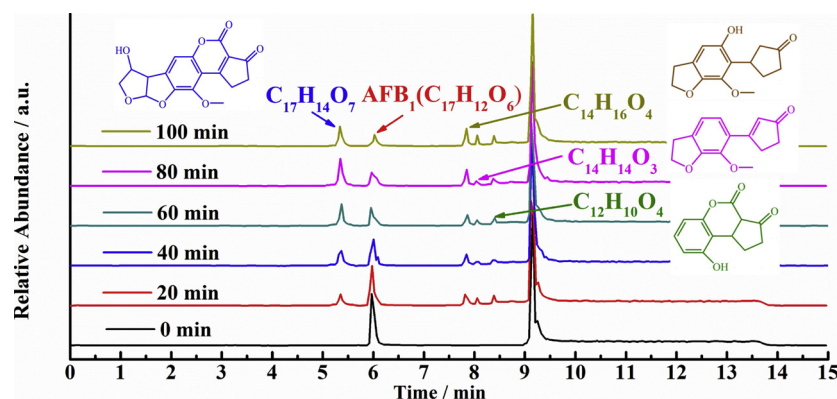

Fig. 4. Total ion chromatogram of intermediate products of AFB$_1$ in aqueous solution over CW-10.83% under visible light irradiation.

Table 1
The nominal level (NL 1×10^6) of AFB$_1$ and four intermediate products in different time.

Time(min)	AFB$_1$ (C$_{17}$H$_{12}$O$_6$)	C$_{17}$H$_{14}$O$_7$	C$_{14}$H$_{16}$O$_4$	C$_{14}$H$_{14}$O$_3$	C$_{12}$H$_{10}$O$_4$
0	39.27	0	0	0	0
20	30.26	8.99	8.78	5.91	6.22
40	20.33	11.63	8.89	4.43	4.73
60	13.11	16.80	8.10	5.12	5.25
80	9.66	20.94	10.23	4.63	6.01
100	8.26	15.26	13.57	8.15	7.56

might slow down sharply. And then AFB$_1$-9-hydroxy may be converted to other intermediate products through ROS reaction with longer irradiation time. This proposed pathway of AFB$_1$ inactivation to AFB$_1$-9-hydroxy could be also inferred through comparing our previous works with present findings. From their MS results, it was found that the NL intensity of AFB$_1$-9-hydroxy was higher in the present of CW-10.83% in 80 min (NL: 20.94×10^6) than that of g-C$_3$N$_4$ in our previous reports (NL: 8.12×10^6 in 120 min) [11], which may be ascribed to that the more ·OH radicals generated in the presence of CW-10.83%. As for g-C$_3$N$_4$, the formation of limited ·OH radicals may be indirectly from ·O$_2^-$ via multi-reactions (O$_2$ + e$^-$ → ·O$_2^-$ + e$^-$ + H$^+$ → H$_2$O$_2$ + e$^-$ → •OH) [42,43], while in the present of CW-10.83% with effective charges separation and electron/hole transfer, a large number of ·OH radicals could generate from directly oxidizing OH$^-$ or H$_2$O to ·OH on the VB of WO$_3$. Therefore, it was deduced that a large number of ·OH radicals produced from this effective photocatalytic system were most likely to react with the C8=C9 to form more AFB$_1$-9-hydroxy, which was further confirmed in following sections.

To confirm the role of active radicals in photocatalytic inactivation of AFB$_1$, the radical trapping experiments and HRMS were conjunctively performed via adding different scavengers into the solution before the photocatalytic process. The $m/z = 331.0813$ was chosen as molecular ion peak of AFB$_1$-9-hydroxy, which was monitored by HRMS under different conditions. In Fig. 5, it was found that the NL of AFB$_1$-9-hydroxy decreased sharply in the presence of tert-butanol (t-BuOH), indicating the ·OH radicals played a very important role in inactivation of AFB$_1$ to AFB$_1$-9-hydroxy. And in the presence of 1,4-benzoquinone (BQ) and the same amount of t-BuOH as the previous trapping test, the inactivation activity of AFB$_1$ to AFB$_1$-9-hydroxy was further restrained, but the inactivation performance is less effective than the ·OH radicals. This indicated that the ·O$_2^-$ active radicals also took part in this inactivation reaction, which might be transferred indirectly to ·OH as mentioned before. Therefore, it could be found from above results that the ·OH radicals were the main reactants for the inactivation of AFB$_1$ to AFB$_1$-9-hydroxy over CW-10.83%.

For deeply understanding the mentioned pathways for the inactivation of AFB$_1$, stable isotope-labeling investigations were carried
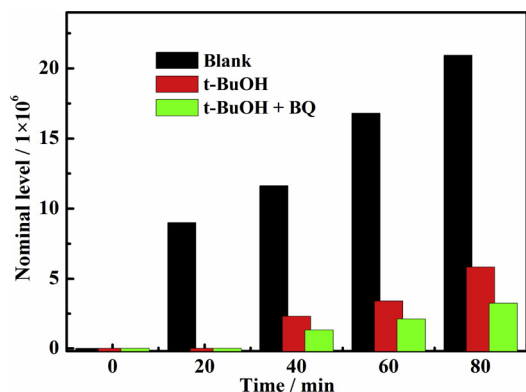
Fig. 5. The nominal level of AFB$_1$-9-hydroxy ($m/z = 331.0813$) with irradiation time in the present of different scavenger conditions over CW-10.83%.

out. Owing to that the participation of the dissolved oxygen and solvent H$_2$O is indispensable in photoreaction, the photocatalytic inactivation of AFB$_1$ were performed using labeled ^{18}O$_2$ (> 97%)/H$_2$^{16}O and 50% H$_2$^{18}O + 50% H$_2$^{16}O in atmospheric condition, respectively. The isotope abundance of the AFB$_1$-9-hydroxy was recorded by HRMS in both conditions, which was shown in Fig. 6. In the presence of ^{18}O$_2$ /H$_2$^{16}O, it could be found that the products contained the isotope peaks of $m/z = 333.09457$ with weaker isotope abundance, which mean that there was one labeled oxygen atom from ^{18}O$_2$ participated in the photoreaction. This further demonstrated that the indirect pathway of ·O$_2^-$ to ·OH (O$_2$ + e$^-$ → ·O$_2^-$ + e$^-$ + H$^+$ → H$_2$O$_2$ + e$^-$ → ·OH) as previous inference was feasible. When the photoreaction was carried out in the 50% H$_2$^{18}O + 50% H$_2$^{16}O with ^{16}O$_2$ from air, the isotope peaks of $m/z = 333.09464$ showed the higher abundance than that of ^{18}O$_2$ /H$_2$^{16}O. Isotope-labeling researches indicated that the more ·OH could be derived from H$_2$^{18}O or ^{18}OH$^-$ oxidation by holes over CW-10.83%, and then attacked the C8=C9 site to form AFB$_1$-9-hydroxy ($m/z = 333.09464$), which was consistent with the trapping test. Therefore, it can be concluded that above experimental results was consistent with the previous proposed mechanism.

3.4. Theoretical calculations

Although the AFB$_1$-9-hydroxy (C$_{17}$H$_{14}$O$_7$) was also identified as one of products in other's works which utilized gamma ray radiation [44], high-voltage atmospheric cold plasma (HVACP) [45] and ozone treatment [46] to degrade AFB$_1$, the reasonable explanations for the formation of AFB$_1$-9-hydroxy were deficient in these studies. Obviously, the reasons for ·OH radical reacting with C9 site rather than other site of AFB$_1$ need deeper confirmation. In order to further confirm the feasibility of above proposed reaction mechanism, theoretical calculations were applied to investigate the hydroxyl radical reaction on AFB$_1$, especially for the toxic site of C8=C9 site. The B3LYP function with the 6-31 + G (d,p) basis set for atoms C, H and O were used to geometry optimization of all the minima and transition states, and the calculations were performed by the Gaussian09 package in water solution. To study the reaction properties of reactants, the optimized configuration and the electrostatic potentials of AFB$_1$ were shown in Fig. 7a and b, respectively. It was found that the strong negative region concentrates on the oxygen atom of lactone and adjacent five-membered ring, while all the unperturbed hydrogen atoms showed positive electrostatic potential especially the hydrogen atom of furan ring double ring (C8=C9) group and methoxyl (OCH$_3$) group.

In the principle of photocatalytic reaction, it was commonly supposed that generated ·OH radicals reacted with adsorbed species via ·OH-addition or hydrogen abstraction reaction in aqueous solution [47,48]. From previous the results of HRMS and ^{18}O isotopic tracing, it was found that the ·OH-addition was more probable between AFB$_1$ and ·OH radicals in initial reaction. Moverover, the ·OH-addition reaction generally occurred at unsaturated carbon bonds [49], which depended strongly on the activity of reactive site. However, among the 17 possible carbon positions, addition reaction on C8=C9 site was most feasible, because the C=C double bond (C9b=C9c, C5a=C5 and C4 = C3b) in benzene ring and C3a=C11a band were associated with strong conjugated π bond, which were more difficult to occur addition reaction than C8=C9. The natural bond orbital (NBO) analysis was used to estimate which unsaturated carbon atom was most potentially attacked by ·OH radicals. The calculated natural atomic charge of C, H, O atoms were recorded in the table of Fig. 8. It could be found that the natural charge of C9 (No. C28 atom) was –0.32938, which was more negative than that of C8 (No. C29 atom, 0.09827). This indicated that, since the ·OH radicals was electrophilic in nature, the ·OH radicals were inclined to attack the C9 site with atomic charges rather than C8 site and other sites.

In addition, the coupling reaction of AFB$_1$ and ·OH radicals was determined by using frontier molecule orbital theory [50]. As shown

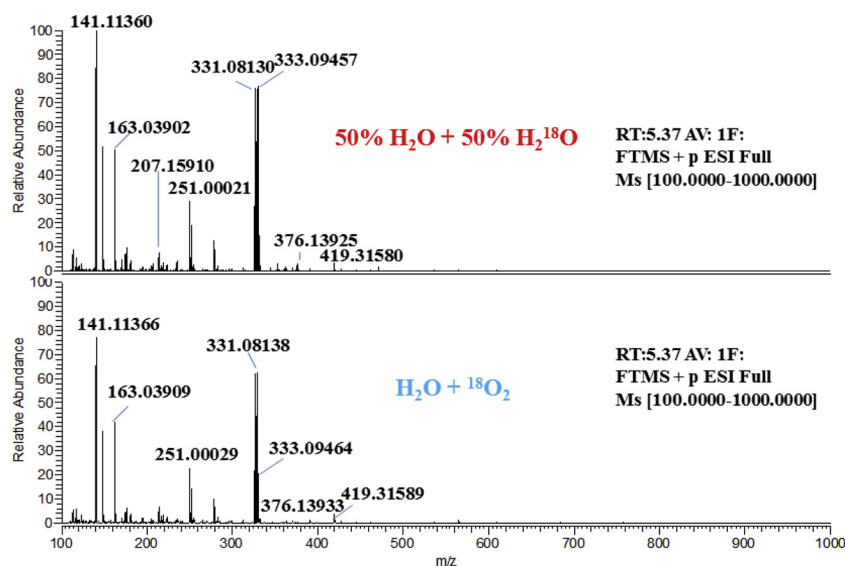**Fig. 6.** Selected ion monitoring of AFB$_1$-9-hydroxy using ^{18}O isotope-labeling over CW-10.83% under visible light irradiation.

the Fig. 9, the highest occupied molecular orbital (HOMO) and the lowest unoccupied molecular orbital (LUMO) of two reactants were calculated and given. It can be found that the largest interaction should occur between the HOMO of AFB$_1$ and the β-LUMO of the ˙OH radicals, and the energy gap was as low as $\Delta E = 1.31$ eV, which suggested that the interaction between these frontier orbitals was very strong. Therefore, based on above theoretical calculations and experimental results, it can be proposed that the ˙OH radical addition can preferentially occur on the C8═C9 double band of AFB$_1$, and the ˙OH radical is most likely to interact with the C9 position.

3.5. Charges transfer mechanism of CdS/WO$_3$ composites

In order to investigate the mechanism of charge transfer over the composites, DRS and Mott-Schottky measures were used to estimate the band structures. As shown in the DRS spectrums (Fig. S7a), WO$_3$ could absorb visible light shorter than 465 nm, while the CdS had the edge of light adsorption at 580 nm. With the increasing content of CdS, a red shift of the absorption edge was observed, which was confirmed by the color of the composites shown in Fig. S7a. The following formula (1) was used to calculate the band-gap:

$$ahv = A \ (hv-E_g)^{n/2} \tag{1}$$

where α, hν, Eg and A are absorption index, light energy, bandgap energy, and constant value of semiconductor, respectively. The n value of CdS and WO$_3$ was 4 (for indirect transition) and 1 (for direct transition), respectively [39,51,52]. The bandgap of pure CdS and WO$_3$ were about 2.14 eV and 2.66 eV, respectively (Fig. S7b). The Mott-Schottky plots of

CdS and WO$_3$ (Fig. S7c) revealed the positive slope in the linear region, indicating that they were n-type behavior [53]. For n-type semiconductors, the bottom edge of CB was close to the flat band potential that could be calculated by the X-intercept. The bottom edge CB of CdS and WO$_3$ were approximately –1.26 V and –0.07 V vs. SCE (Saturated calomel electrode) at pH7.00, respectively. After calculation based on the formula (2), (3), the CB and VB of CdS were measured to be –0.61 V and 1.53 V (vs. NHE, pH0.0), while that of WO$_3$ were 0.58 V and 3.24 V (vs. NHE, pH0.0), respectively.

$$E(vs. \ NHE, \ pH = 0) = E(vs. \ SCE, \ pH = 7) + 0.0591pH + 0.24 \ V \tag{2}$$

$$E_{CB} = E_{VB} - E_g \tag{3}$$

The ESR measurement was also used to detect directly the formation of ˙O$_2^-$ and ˙OH radicals. It was found that no any characteristic peaks could be detected under dark condition over CW-10.83%. Moreover, the ˙O$_2^-$ signals over WO$_3$ and the ˙OH radicals signals in the presence of CdS were hardly detected under visible light irradiation, respectively, which were consistent with the detection of ˙O$_2^-$ and ˙OH (Fig. 3c and d). This was due to that the potential of CB in WO$_3$ was more positive than the potential of O$_2$/˙O$_2^-$ (–0.33 V vs NHE), and the potential of VB in CdS was more negative than that of OH$^-$/˙OH (+2.4 V vs NHE) [55–57]. As depicted in Fig. 10a and Fig. 10b, the characteristic peaks of DMPO-˙O$_2^-$ and DMPO-˙OH adducts could be observed under visible light irradiation, and the intensity of characteristic signal increased with time, indicating that continuous ˙O$_2^-$ and ˙OH radicals formed during the reaction. However, the heterojunction-type could not explain the above radical generation as the previous study [54]. If the photogenerated electrons from CB of CdS
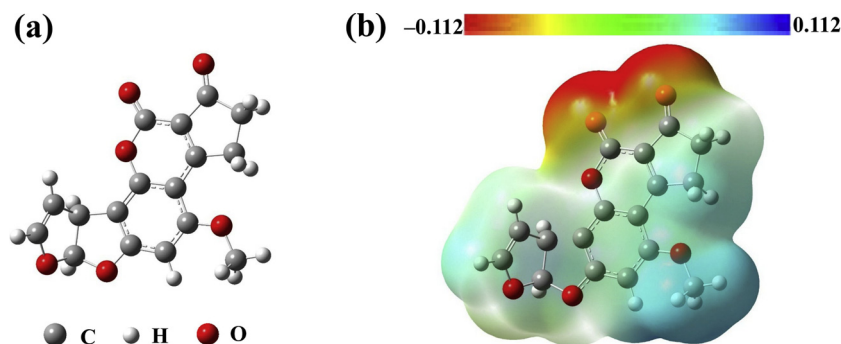

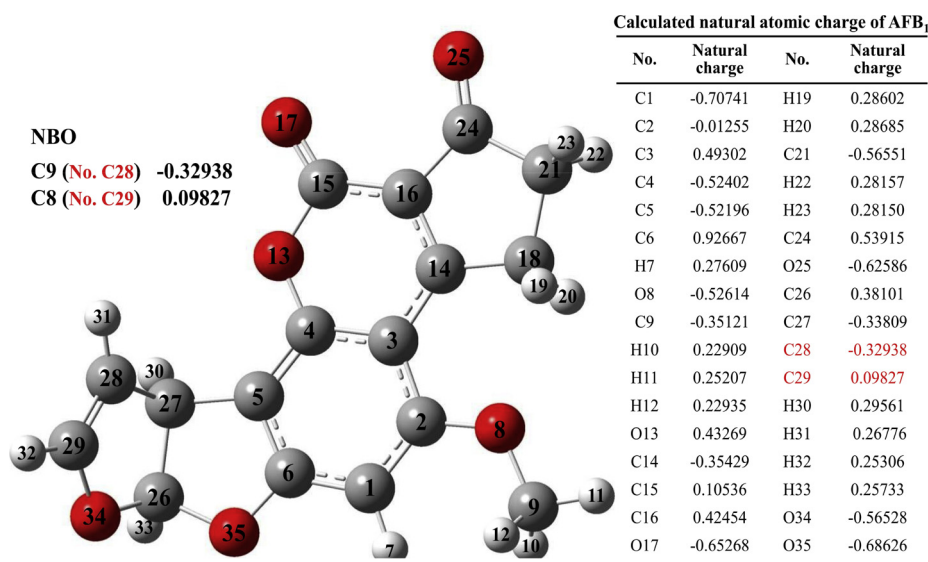**Fig. 7.** Optimized geometry (a) and molecular electrostatic potential map of AFB$_1$ (b).

Calculated natural atomic charge of AFB$_1$

No.	Natural charge	No.	Natural charge
C1	-0.70741	H19	0.28602
C2	-0.01255	H20	0.28685
C3	0.49302	C21	-0.56551
C4	-0.52402	H22	0.28157
C5	-0.52196	H23	0.28150
C6	0.92667	C24	0.53915
H7	0.27609	O25	-0.62586
O8	-0.52614	C26	0.38101
C9	-0.35121	C27	-0.33809
H10	0.22909	C28	-0.32938
H11	0.25207	C29	0.09827
H12	0.22935	H30	0.29561
O13	0.43269	H31	0.26776
C14	-0.35429	H32	0.25306
C15	0.10536	H33	0.25733
C16	0.42454	O34	-0.56528
O17	-0.65268	O35	-0.68626

NBO

C9 (No. C28) -0.32938
C8 (No. C29)   0.09827

Fig. 8. The atomic charge of C, H, O in AFB$_1$ from natural bond orbital (NBO).

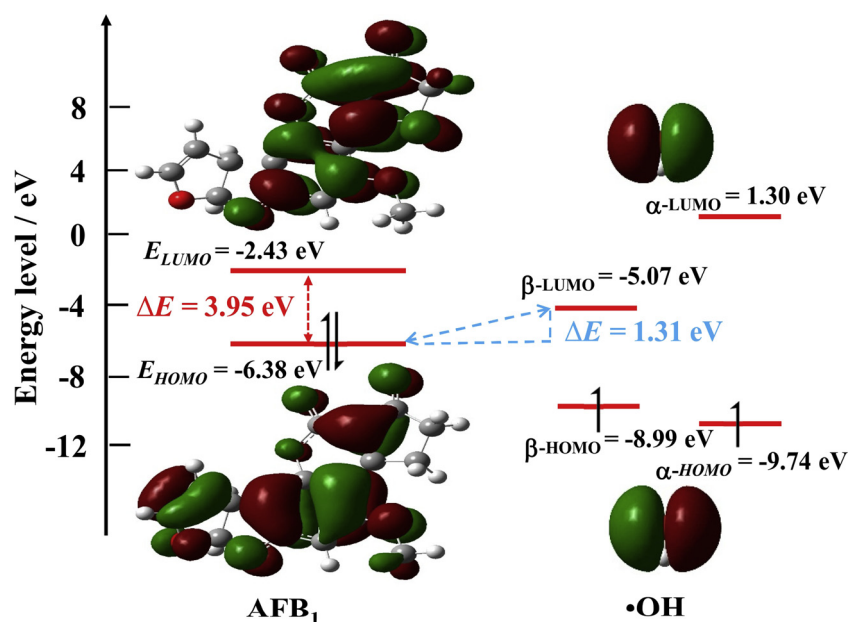**Fig. 9.** Molecular orbitals and electron distribution in the frontier orbitals of the reaction partners for the ˙OH radical addition to AFB$_1$.

transferred to the CB of WO$_3$, the electrons on the CB of WO$_3$ cannot reduce absorbed O$_2$ to form ˙O$_2^-$ radicals. In addition, the holes on the VB of CdS also can not promote the formation of ˙OH radicals. Therefore, it could be concluded that the mechanism of CdS/WO$_3$ composites should be direct Z-scheme (Fig. 10c). In this case, the electrons in the CB of WO$_3$ would transfer and recombine with the holes from the VB of CdS, leading to facilitate efficient charges separation of each component. Then, the electrons on the CB of CdS and holes on the VB of WO$_3$ accumulated and participated in the formation of ˙O$_2^-$ and ˙OH radicals. Thus, not only the photocatalytic efficiency was improved by the excellent separation of charges, but also the better redox ability can be utilized to produce more radicals.

Based on above discussions and conclusions, we proposed that the CdS/WO$_3$ composites presented all-solid-state Z-scheme system for preferentially photocatalytic inactivating the toxic site of AFB$_1$, shown in Scheme 2. Under visible light irradiation, CdS and WO$_3$ were excited to generate the e$^-$/h$^+$ pairs. The e$^-$ in the CB of WO$_3$ could directly transfer and recombine with h$^+$ in the VB of CdS. Then, the e$^-$ and h$^+$

with high energy on the CdS and WO$_3$ actuated the photocatalytic redox processes, respectively. The h$^+$ on the WO$_3$ could directly oxide the OH$^-$ or H$_2$O to generate ˙OH, while the e$^-$ on CdS could reduce O$_2$ to ˙O$_2^-$, and then indirectly to form ˙OH. These ˙OH radicals rapidly and preferentially attacked C9 site of the unsaturated double band C8=C9 in AFB$_1$, and then undergo electron and proton transfer [58,59] to form AFB$_1$-9-hydroxy. Most important, in order to prove the efficient inactivation of toxic site, the cytotoxicity of intermediates and products were investigated by cell viability assay (Cell Counting Kit-8). It could be found from Fig. S8 that the viability of L-02 liver cells reduced weekly in the present of intermediates and products, while the cell viability decreased sharply under AFB$_1$ treatment. This indicated that the main hypertoxic site (C8=C9 double band) of AFB$_1$ was inactivated during photoreaction, and the present photocatalytic system was a promising and high-efficiency for reducing toxicity or risk of AFB$_1$.
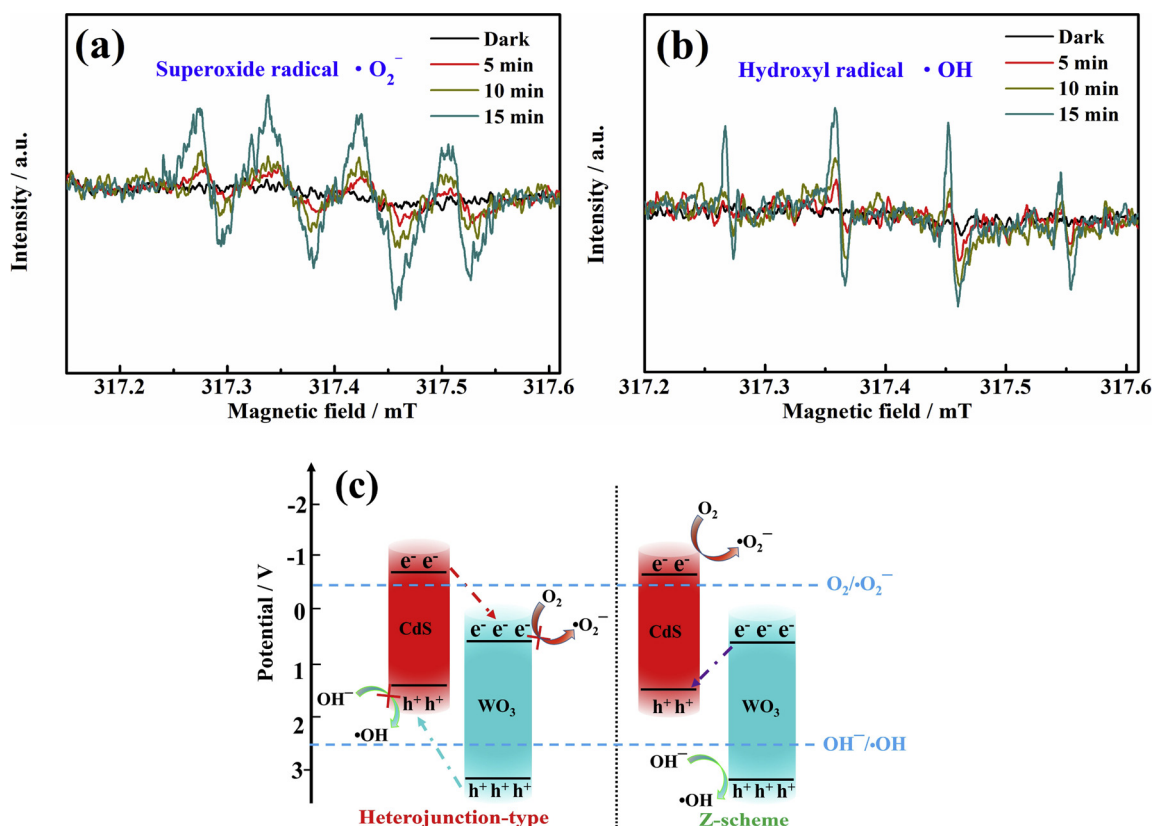
Fig. 10. DMPO-˙O_2^- (a) and DMPO-˙OH (b) trapping ESR spectra in the presence of CW-10.83% under visible light, charge transfer pathway of the composites (c).

4. Conclusion

In summary, the photocatalytic inactivation mechanism of hypertoxic site in AFB_1 was verified through theoretical and experimental evidences. Clew-like WO_3 decorated with CdS nanoparticles were successfully prepared by microwave-assisted hydrothermal and precipitation method, which showed excellent activities for inactivating hypertoxic site C8＝C9 under visible light irradiation resulting in a sharp decrease of toxicity. This efficient Z-schematic composite not only promoted the charge separation and prolong the life time of charges, but also utilized the well oxidation ability of WO_3 to oxidize the OH^- to ˙OH, which were the key active radicals for photocatalytic inactivation. The reaction mechanism of ˙OH radicals with C8＝C9 were confirmed systematically through the structure identification of intermediates, radical trapping, ^{18}O isotope labeling. And DFT theoretical calculations illuminated that ˙OH radicals were inclined to react with the C9 site rather than other sites. Our finding can be as a theoretical direction for design of efficient photocatalyst to mitigate highly toxic pollutant in future study.

Acknowledgements
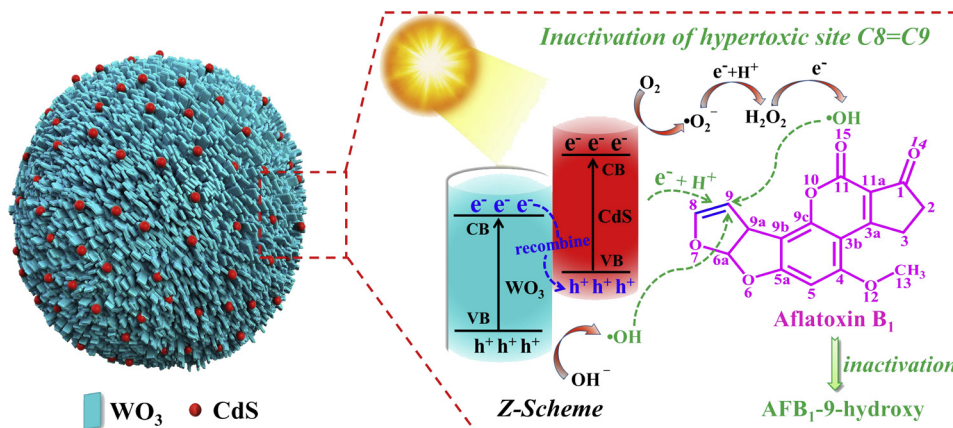
Scheme 2. Illustration of the proposed mechanism over CdS/WO_3 composites for inactivating the hypertoxic site (C8＝C9) in AFB_1 under visible light irradiation.

Appendix A. Supplementary data

Supplementary material related to this article can be found, in the online version, at doi:https://doi.org/10.1016/j.apcatb.2019.01.057.

References

[1] D. Conradt, M.A. Schätzle, J. Haas, J. Am. Chem. Soc. 137 (2015) 10867–10869.
[2] B.W. Horn, J Toxical-Toxin Rev. 22 (2003) 351–379.
[3] R.M. Elsanhoty, I.A. Al-Turki, M.F. Ramadan, Water Sci. Technol. 74 (2016) 625–638.
[4] L.L. Bedard, T.E. Massey, Cancer Lett. 241 (2006) 174–183.
[5] P.C. Turner, A. Sylla, Y.Y. Gong, M.S. Diallo, A.E. Sutcliffe, A.J. Hall, C.P. Wild, Lancet 365 (2005) 1950–1956.
[6] Y.C. Lin, N. Owen, I.G. Minko, S.S. Lange, J.Y. Tomida, L. Li, M.P. Stone, R.D. Wood, A.K. McCullough, R.S. Lloyd, PNAS 113 (2016) 13774–13779.
[7] Y. Liu, C.C.H. Chang, G.M. Marsh, F. Wu, Eur. J. Cancer 48 (2012) 2125–2136.
[8] F. Wang, F. Xie, X.F. Xue, Z.D. Wang, B. Fan, Y.M. Ha, J. Hazard. Mater. 192 (2011) 1192–1202.
[9] X.H. Luo, R. Wang, L. Wang, Y.F. Li, Y.Y. Bian, Z.X. Chen, Food Control 37 (2014) 171–176.
[10] H.Z. Lorestani, O. Sabzevari, N. Setayesh, M. Amini, A.N. Ahmadabadi, M.A. Faramarzi, Chemosphere 135 (2015) 1–6.
[11] J. Mao, L.X. Zhang, H.T. Wang, Q. Zhang, W. Zhang, P.W. Li, Chem. Eng. J. 342 (2018) 30–40.
[12] P. Zhou, J. Yu, M. Jaroniec, Adv. Mater. 26 (2014) 4920–4935.
[13] F. Ye, H.F. Li, H.T. Yu, S. Chen, X. Quan, Appl. Catal. B: Environ. 227 (2018) 258–265.
[14] X. Jia, M. Tahir, L. Pan, Z.F. Huang, X.W. Zhang, L. Wang, J.J. Zou, Appl. Catal. B: Environ. 198 (2016) 154–161.
[15] F.Q. Zhou, J.C. Fan, Q.J. Xu, Y.L. Min, Appl. Catal. B: Environ. 201 (2017) 77–83.
[16] P. Li, Y. Zhou, H.J. Li, Q.F. Xu, X.G. Meng, X.Y. Wang, M. Xiao, Z.G. Zou, Chem. Commun. 51 (2015) 800–803.
[17] J. Yan, T. Wang, G. Wu, W. Dai, N. Guan, L. Li, J. Gong, Adv. Mater. 27 (2015) 1580–1586.
[18] W.J. Li, P.M. Da, Y.Y. Zhang, Y.C. Wang, X. Lin, X.G. Gong, G.F. Zheng, ACS Nano 8 (2014) 11770–11777.
[19] X.Y. Chen, Y. Zhou, Q. Liu, Z.D. Li, J.G. Liu, Z.G. Zou, ACS Appl. Mater. Interfaces 4 (2012) 3372–3377.
[20] X.K. Zeng, Z.Y. Wang, G. Wang, T.R. Gengenbach, D.T. McCarthy, A. Deletic, J.G. Yu, X.W. Zhang, Appl. Catal. B: Environ. 218 (2017) 163–173.
[21] J. Zhang, Y. Ma, Y.L. Du, H.Z. Jiang, D.D. Zhou, S.S. Dong, Appl. Catal. B: Environ. 209 (2017) 253–264.
[22] L.F. Cui, X. Ding, Y.G. Wang, H.C. Shi, L.H. Huang, Y.H. Zuo, S.F. Kang, Appl. Surf. Sci. 391 (2017) 202–210.
[23] Z.Y. Jin, N. Murakami, T. Tsubota, T. Ohno, Appl. Catal. B: Environ. 150–151 (2014) 479–485.
[24] S.S. Acharyya, S. Ghosh, R. Bal, Chem. Commun. (Camb.) 51 (2015) 5998–6001.
[25] J.J. Yang, D.M. Chen, Y. Zhu, Y.M. Zhang, Y.F. Zhu, Appl. Catal. B: Environ. 205 (2017) 228–237.
[26] B.B. Liu, X.J. Liu, J.Y. Liu, C.J. Feng, Z. Li, C. Li, Y.Y. Gong, L.K. Pan, S.Q. Xu, C.Q. Sun, Appl. Catal. B: Environ. 226 (2018) 234–241.
[27] J. Jin, J.G. Yu, D.P. Guo, C. Cui, W. Ho, Small 11 (2015) 5262–5271.
[28] A.H. Yan, C.S. Xie, D.W. Zeng, S.Z. Cai, H.Y. Li, J. Alloys. Compd. 495 (2010) 88–92.
[29] N. Wang, D.G. Wang, M.R. Li, J.Y. Shi, C. Li, Nanoscale 6 (2014) 2061–2066.
[30] Z. Jiao, J. Wang, L. Ke, X.W. Sun, H.V. Demir, ACS Appl. Mater. Interfaces 3 (2011) 229–236.
[31] J. Mao, B. He, L.X. Zhang, P.W. Li, Q. Zhang, X.X. Ding, W. Zhang, Toxins 8 (2016) 332.
[32] M.J. Frisch, G.W. Trucks, H.B. Schlegel, G.E. Scuseria, M.A. Robb, J.R. Cheeseman, G. Scalmani, V. Barone, B. Mennucci, G.A. Petersson, H. Nakatsuji, Gaussian 09, Revision D. 01, Gaussian, Inc., Wallingford, CT, 2013.
[33] A.D. Becke, J. Chem. Phys. 98 (1993) 5648–5652.
[34] C.T. Lee, W.T. Yang, R.G. Parr, Phys. Rev. B 37 (1988) 785–789.
[35] V. Barone, M. Cossi, J. Tomasi, J. Chem. Phys. 107 (1997) 3210.
[36] J. Tomasi, B. Mennucci, R. Cammi, Chem. Rev. 105 (2005) 2999–3094.
[37] T.M. Perecto, C.A. Zito, D.P. Volanti, CrystEngComm 19 (2017) 2733–2738.
[38] D. Chen, J.H. Ye, Adv. Funct. Mater. 18 (2008) 1922–1928.
[39] L.J. Zhang, S. Li, B.K. Liu, D.J. Wang, T.F. Xie, ACS Catal. 4 (2014) 3724–3729.
[40] P.Q. Zhao, S.J. Xiong, X.L. Wu, P.K. Chu, Appl. Phys. Lett. 100 (2012) 171911.
[41] J.C. Oguma, Y. Kakuma, S. Murayama, Y. Nosaka, Appl. Catal. B: Environ. 129 (2013) 282–286.
[42] S.Z. Wu, K. Li, W.D. Zhang, Appl. Surf. Sci. 324 (2015) 324–331.
[43] F. Dong, Z.Y. Wang, Y.H. Li, W.K. Ho, S.C. Lee, Environ. Sci. Technol. 48 (2014) 10345–10353.
[44] F. Wang, F. Xie, X.F. Xue, Z.D. W, B. Fan, Y.M. Ha, J. Hazard. Mater. 192 (2011) 1192–1202.
[45] H. Shi, B. Cooper, R.L. Stroshine, K.E. Ileleji, K.M. Keener, J. Agric. Food Chem. 65 (2017) 6222–6230.
[46] X.H. Luo, R. Wang, Y.F. Li, R.H. Zheng, X.L. Sun, Y. Wang, Z.X. Chen, G.J. Tao, Food Addit. Contam. Part A Chem. Anal. Control Expo. Risk Assess. 31 (2014) 105–110.
[47] Y. Nosaka, A.Y. Nosaka, Chem. Rev. 117 (2017) 11302–11336.
[48] H. Fang, Y.P. Gao, G.Y. Li, J.B. An, P.K. Wong, H.Y. Fu, S.D. Yao, X.P. Nie, T.C. An, Environ. Sci. Technol. 47 (2013) 2704–2712.
[49] S. Banerjee, S.C. Pillai, P. Falaras, K.E. O'Shea, J.A. Byrne, D.D. Dionysiou, J. Phys. Chem. Lett. 5 (2014) 2543–2554.
[50] K. Fukui, T. Yonezawa, H. Shingu, J. Chem. Phys. 20 (2004) 722.
[51] S.A. Ivanov, A. Piryatinski, J. Nanda, S. Tretiak, K.R. Zavadil, W.O. Wallace, D. Werder, V.I. Klimov, J. Am. Chem. Soc. 129 (2007) 11708–11719.
[52] P.P. González-Borrero, F. Sato, A.N. Medina, M.L. Baesso, A.C. Bento, G. Baldissera, C. Persson, G.A. Niklasson, C.G. Granqvist, Appl. Phys. Lett. 96 (2010) 061909.
[53] L. Zhang, Y.G. Li, Q.H. Zhang, H.Z. Wang, CrystEngComm 15 (2013) 5986–5993.
[54] F. Chen, Q. Yang, J. Sun, F. Yao, S. Wang, Y. Wang, X. Wang, X. Li, C. Niu, D. Wang, G. Zeng, ACS Appl. Mater. Interfaces 8 (2016) 32887–32900.
[55] K. Li, Z. Huang, X. Zeng, B. Huang, S. Gao, J. Lu, ACS Appl. Mater. Interfaces 9 (2017) 11577–11586.
[56] M. Mrowetz, W. Balcerski, A.J. Colussi, M.R. Hoff ;mann, J. Phys. Chem. B 108 (2004) 17269–17273.
[57] Z. Zhang, D. Jiang, D. Li, M. He, M. Chen, Appl. Catal. B: Environ. 183 (2016) 113–123.
[58] X.J. Li, W.S. Jenks, J. Am. Chem. Soc. 122 (2000) 11864–11870.
[59] Y. Ma, X.L. Wang, Y.S. Jia, X.B. Chen, H.X. Han, C. Li, Chem. Rev. 114 (2014) 9987–10043.